Original Article

Nonconventional synthesis of polyhedral Mn_3O_4 nanoarchitectures incorporated reduced graphene oxide: superior supercapacitor capabilities

Mohamed Mokhtar Mohamed [a,**], M. Khairy [b,c,*], Ahmed A. Amer [b], M.A. Mousa [b]

[a] Egypt-Japan University of Science and Technology, Borg El Arab, Alexandria 21934, Egypt
[b] Chemistry Department, Faculty of Science, Benha University, Benha, Egypt
[c] Chemistry Department, College of Science, Imam Mohammad Ibn Saud Islamic University (IMSIU), Riyadh 11623, Saudi Arabia

ABSTRACT

Mn_3O_4/graphene nanocomposites with different ratios (M1G1, M1G3 and M3G1) were successfully synthesized by a deposition-solvothermal process. The composites were well characterized with different tools such as TEM-SAED, XRD, FTIR, Raman techniques, and N_2 adsorption. The electrochemical characteristics of the nanocomposites were evaluated using cyclic voltammetry (CV), galvanostatic charge-discharge (GCD), and impedance spectroscopy in comparison to pure Mn_3O_4. Mn_3O_4 nanoarchitectures (15 nm) and their interaction with graphene, indicating the well-dispersion of Mn_3O_4 in graphene, were confirmed via TEM-SAED. The M3G1 composite, which contains mostly Mn_3O_4 and Mn_2O_3 moieties, has the largest specific capacitance of 490 F g^{-1} at current density of 0.25 A g^{-1}, the highest power density of 2412 W kg^{-1}, a considerable energy density of 45 Wh kg^{-1}, and exceptional cycling stability of 0% loss after 1000 cycles. The quick charge diffusion mechanism, high surface area, and pore volume were all influencing factors.

1. Introduction

The demand for a renewable energy storage system has risen dramatically as a result of the fast development of various electronic gadgets such as electric automobiles and mobile batteries. EDLCS and pseudocapacitor supercapacitors are incredibly promising electrochemical devices for both storing and releasing energy [1—5]. RuO_2 is a noble oxide with exceptional chemical and electrical characteristics, as well as a high theoretical capacitance value (2000 F g^{-1}) [6]. However, it was never used for storing or releasing material due to some disadvantages, most importantly its high cost and toxicity [7]. Accordingly, researchers have made an extensive search for

alternative materials, for instance MnO_x and Fe_3O_4 and others [8—16]. Because of their high reliability, high theoretical capacitance, long cycle lifetime, and environmentally friendly character, they have been carefully investigated as electrode materials for use in redox-based pseudocapacitors. Their energy storage capabilities for practical applications have been limited by their high electrical resistance and low electrochemical reversibility [17—19]. Due to the various mixed oxidation states of manganese, we were very much drawn to one of the most stable tetragonal forms, named Mn_3O_4 of Mn^{3+} and Mn^{2+} possible transitions and their magnificent applications [20—22]. Expectedly, based on such multiple electroactive cations, a high specific capacitance is expected, as shown previously for the mixed valence Mn^{4+}/Mn^{+3} cations [22]. However, the work done using Mn_3O_4 was uncommon and rather indicates very low capacitance values due to lowering the electrical conductivity value [6]. Designing polyhedral and/or octahedral structures with electroactive spots capable of enhancing electrochemical capacitive performance [23,24] is one technique to overcome such an intrinsic defect. On the other hand, forming a composite or hybrid with carbon-containing materials and specifically carbon nanotubes and activated carbons has improved the conductivity and thus enhanced the specific capacitance values. Liu et al., for example, used a solvothermal approach to successfully manufacture Mn_3O_4—MWCNTs composite with a specific capacitance value of 330 F g^{-1}, which is 18 times higher than a pristine MWCNT [25]. Yuan et al. also devised a simple microwave process for synthesizing Mn_3O_4-mesoporous carbon, which produced a specific capacitance of 266 F g^{-1} at a sweep rate of 1 mV s^{-1} but lost 25.8% of its capacitance after 1000 cycles [26]. Chen et al. recently published a paper describing a new dip-casting approach for producing Mn_3O_4 nanoparticles on a millimetre-long carbon nanotube with a specific capacitance of 143 Fg^{-1} [27]. Previous nanocomposites have high contact resistance at the electrode/current collector, as well as complicated synthetic techniques and high costs, which limit their production and applications. The recommendation of graphene, which has magnificent qualities such as its enormous specific surface area, great chemical stability, and exceptional electrical conductivity, was made in search of more realistic support other than those discussed previously for deploying Mn_3O_4 on its surface [28,29]. Accordingly, researchers have focused on hybrid materials based 'on graphene for the aforementioned synergistic advantages. In this sense, graphene/Mn_3O_4 composites prepared by a simple hydrothermal process showed higher capacitance consisting of four times the power density of individual analogue as well as high retention cycling [30]. Nanosized Mn_3O_4 distributed over graphene produced by combining MnO_2 organosol with ethylene glycol in 6 M KOH and 1 M Na_2SO_4 electrolytes has a specific capacitance of 256 F g^{-1} and 175 F g^{-1} [31], respectively. 6.9% Mn_3O_4/reduced graphene oxide hydrogel with three-dimensional (3D) networks was created through a hydrothermal self-assembly process and demonstrated outstanding cycling stability with no deterioration after 1200 cycles [32]. The close amalgamation of Mn_3O_4-graphene nanocomposites generated via a feasible solution-based synthetic method demonstrated pseudocapacitive activity

with a high specific capacitance (236.7 F g^{-1} at 1 A g^{-1}) and excellent cyclability [33]. On the other hand, the Mn_3O_4—RGO nanocomposite created via a chemical degradation method has a specific capacitance of 131 F g^{-1} in Na_2SO_4 electrolyte (1 M) at 0.5 A g^{-1}. However, numerous disadvantages, such as limited electrolyte accessibility, high concentrations of irreversible structural flaws in the lattices of GO and RGO, unpredictable particle sizes, and effective loading of the nanoparticles, hampered the ability of such hybrids to act as supercapacitors [34—36].

Accordingly, for improving the potential of the energy storage capacity of supercapacitors based on increasing the intrinsic conductivity and surface texturing, we designed a polyhedral Mn_3O_4 nanostructure capable of providing excessive electroactive centers. That upon hybridization with low crystallographic defect graphene oxides showed unprecedented enhancement in the electrochemical capacitance performances. Accordingly, these nanocomposites formed via a deposition-solvothermal process were thoroughly characterized using XRD, TEM-SAED, N_2 sorptiometry, FT-IR and Raman techniques to stand on the reasons behind enhancing their supercapacitive values.

2. Experimental section

All the materials used were analytical grade. H_2SO_4 $NaNO_3$ $KMnO_4$ H_2O_2 hydrazine hydrate [99%, purchased from SDFCL India] $NH_3.H_2O$ (27 wt%) [Obtained from Adwic pharmaceutical and chemicals company Egypt], manganese acetate $Mn(CH_3COO)_2·4H_2O$ [98% was purchased from BDH], DMF [N,N′ dimethylformamide (DMF) were purchased from SDFCL India],

3. Preparation of materials

3.1. Preparation of reduced graphene oxide

The modified Hummers' method was used to prepare graphene oxide from graphite [37]. 5 g of graphite powder was mixed with concentrated sulphuric acid (H_2SO_4, 115 ml, 98 wt %, in a dry ice bath). Then add 2.5 g of sodium nitrate ($NaNO_3$) to the solution, followed by 15 g of potassium permanganate ($KMnO_4$), stirring constantly for 2 h at roughly 10 °C, then 1 h at 35 °C. In an ice bath, 250 ml de-ionized (DI) water was added to the paste. This causes the temperature to rise to 98 °C for 10 min, changing the color of the paste to an orange-yellow hue. After allowing the mixture to cool to room temperature, 50 ml of H_2O_2 was mixed and heated to for 30 min at 90 °C. The resulting mixture was centrifuged and rinsed with hot water numerous times until the pH of the filtrate was neutral. After sonicating the obtained graphene oxide for 30 min in 30 ml distilled water, the reduced graphene oxide was obtained. The obtained mixture was heated at 100 °C and then 3 ml hydrazine hydrate was added to it. The temperature was kept at 100 °C for 24 h and the obtained black reduced graphene was filtrated and then washed several times with distilled water. Vacuum filtration was used to collect the final product, which was then dried at 80 °C.

3.2. Synthesis of Mn_3O_4

Ammonia solution (40 ml) and 100 ml of a 20 mmol ethanolic solution of manganese acetate were mixed under stirring, forming a light red solution. The solution was heated up for 5 min to 50 °C. During this process, deep black suspension was obtained and finally decomposed to form a colloidal solution. The nano-sized Mn_3O_4 crystals were centrifuged and dried at 50 °C.

3.3. Synthesis of RGO/Mn_3O_4

The solvothermal method was used for the preparation of RGO/Mn_3O_4 composites by sonication of 200 ml DMF containing 20 mg RGO, heated to 80 °C for 30 min 20 ml of a 0.2 M manganese acetate solution was added to the above solution and stirred for 1 h to prepare different composites. The obtained precipitate was centrifuged and severally washed with distilled water. Then the final precipitate was added to 200 ml of distilled water and transferred to an autoclave for 10 h at 180 °C. The obtained products were centrifuged using ethanol. Finally, the precipitate dried for 48 h at 60 °C. The obtained precipitates were symbolized as M1G1, M1G3 and M3G1 where M and G are equivalent to M_3O_4 and graphene, respectively; e.g., M3G1 signifies a sample with a weight ratio of 3:1 of Mn_3O_4/reduced graphene oxide.

3.4. Characterization

The resulting nanocomposites were characterized by XRD that measured on Philips 321/00 equipment employing Ni-filtered Cu-Kα radiation (λ = 1.541 Å) at 36 kV in 2θ ranges of 5-80°. Average radius of pore, total volume of pore (V_p), and surface area (BET), were calculated using nitrogen adsorption isotherms recorded by means of traditional volumetric apparatus (r) at −196 °C. BJH analysis of the desorption branch of the isotherm was also used to derive the pore size distribution. With a resolution of 2 cm^{-1} a PerkinElmer Spectrometer with a double beam was used to analyze the Fourier transform infrared (FT-IR) spectra using the KBr method. A Raman spectrometer (U-1000 laser) was utilized to record the Raman spectra using the excitation beam of Ar + emission line at 514.5 nm. TEM-SAED photoimages were recorded by means of a FEI Tecnai G2 F20, Super Twin, at 200 KV accelerating voltage.

3.5. Electrochemical measurements

The electrochemical behavior of free Mn_3O_4 and the Mn_3O_4/graphene nanocomposites (M_xG_x) were thoroughly explored; at room temperature, using PGSTAT204 equipped with Nova 1.11 software for data calculation. Three electrode cell in the presence of 1.0 M of Na_2SO_4 as electrolyte was used, which
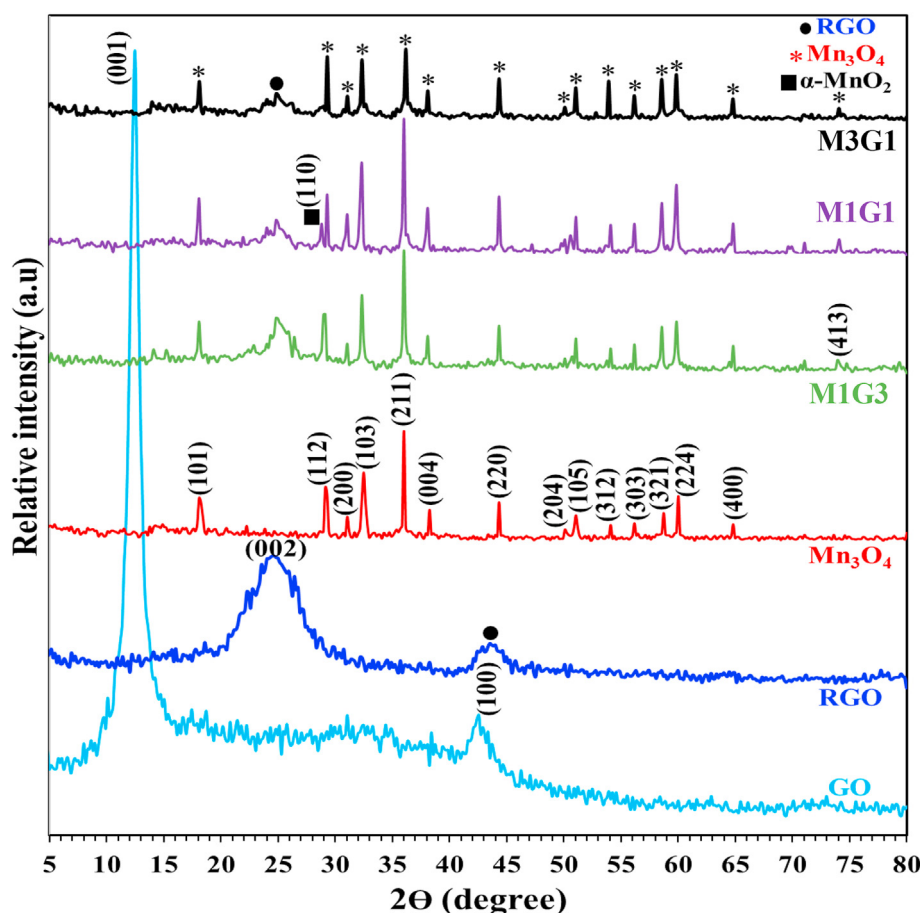

Fig. 1 — XRD patterns of RGO, Mn_3O_4, M1G3, M1G1 and M3G1.

consists of a counter electrode made of platinum, the reference electrode, a saturated calomel electrode (Hg/Hg_2Cl_2), and the working electrode. The working electrode was made by combining the produced nanomaterials (85 wt%) with a binder of 5 wt% Poly (vinylidene fluoride) and a black carbon (10 wt%) with a mass loading of 20 mg/cm^2. The Fluorine tin oxide (FTO) conductive glass sheets [which were purchased from Sigma-Aldrich USA] with an electrical resistance of 14 Ω cm^{-2} and dimensions equal to 1 cm^2 were cleaned and dried. The above-prepared paste was then distributed with a doctor blade and uniformly rolled over FTO glass. Finally, the paste applied to FTO was dried for 3 h at 200 °C. CVs were performed between -0.85 and $+0.65$ V with scan rates of 10, 20, 50, and 100 mV s^{-1}. Electrochemical impedance spectroscopy was used to determine the charge transfer efficiency of electrodes (EIS). The electrochemical impedance was measured with the PGSTAT204 in the frequency range of 0.1 Hz–140 kHz, with a constant potential of 10 mV and currents ranging from 10 to 100 mA. The impedance spectra were confirmed using the Kramers-Kronig transformation. The specific capacitance was determined using galvanostatic charge-discharge and chronopotentiometry using a Digi-Ivy 2116 B-USA equipped with DY2100B software for data computation. Working electrodes were made at potentials ranging from -0.85 to $+0.65$ V and current densities of 0.25, 0.5, and 1 mA g^{-1}.

4. Results and discussion

4.1. XRD and TEM-SAED analysis

Fig. 1 depicts the diffraction patterns using X-ray (XRD) of pure Mn_3O_4 nanoparticles, graphene oxide, reduced graphene oxide (RG), and Mn_3O_4/RG nanocomposites. The appearance of RG diffraction peaks related to (002) and (100) reflections at longer angles of $2\theta = 24.5°$ and $43.8°$ characteristic of graphite carbon, as well as the disappearance of the diffraction peak of graphene oxide at $12.5°$, indicate that graphene oxide was reduced at an average interlayer distance of 3.63 Å during the hydrazine-thermal process. Reduced graphene (RG) stacking is indicated by broadening the peaks of graphene oxide following reduction. The Mn_3O_4 sample shows XRD pattern with lots of sharp peaks attributed to the (101), (112), (200), (103), (211), (004), (220), (204), (105), (312), (303), (321), (224) and (400) planes that are corresponding to the tetrahedral Hausmannite Mn_3O_4 with space group I41/amd well matched with
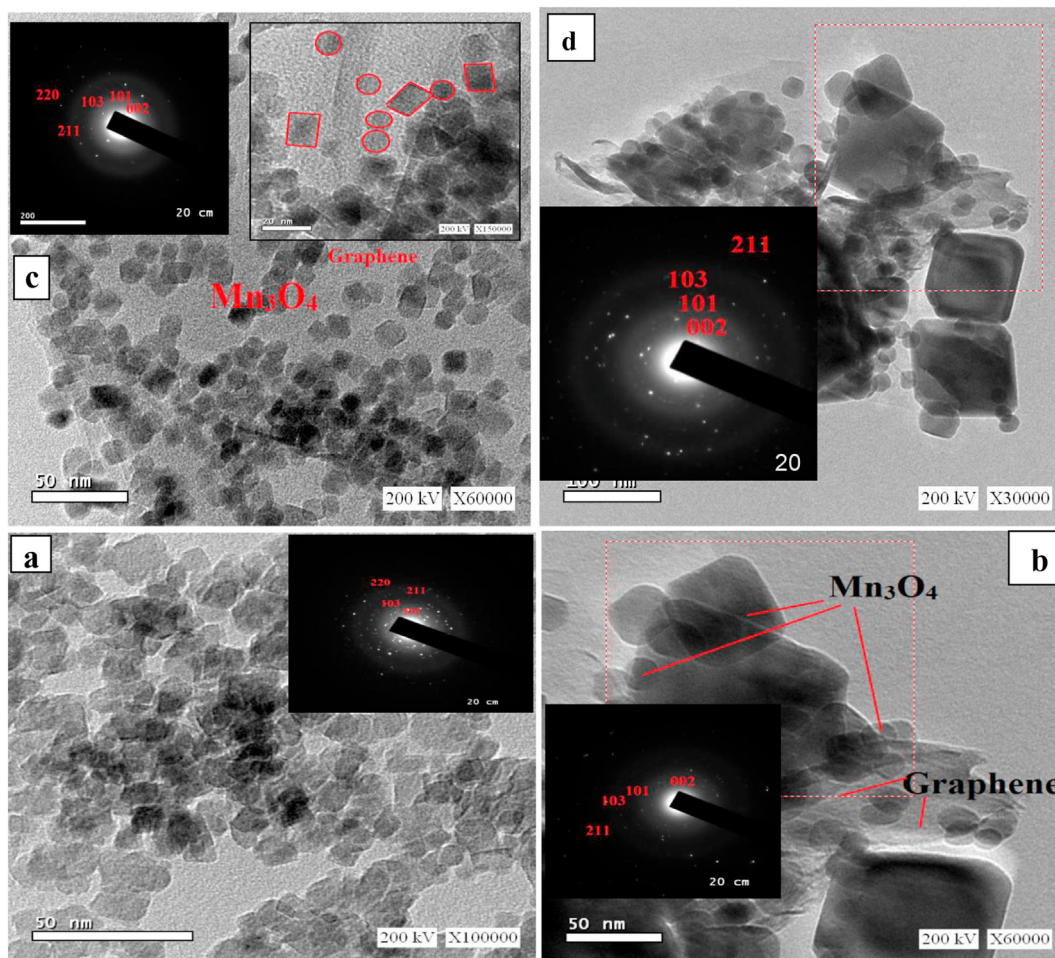

Fig. 2 – TEM Images of (a) Mn₃O₄ (b) M1G1 and (C) M3G1 and M1G3 (D) together with their corresponding magnified HRTEM images and SAED patterns, as insets.

JCPDS No. 24—0734. The average crystallite size of Mn_3O_4 is 15 nm which is determined from Sherrer's equation [38].

The XRD pattern of Mn_3O_4/RG nanocomposites reveals the peaks related to each of RG and Mn_3O_4 phase. It was observed that all nanocomposites reveal disappearance of the peak of RG related to (100) pl]ane, indicating in-plane crystallite site activity. As the ratio of Mn_3O_4 increases relative to RG as in M1G1 and M3G1 samples as the order of graphene sheets decreases, causing splitting and deterioration of the (002) peak. The XRD patterns of M1G3 and M1G1 displayed enhanced crystallinity in the Mn_3O_4 Hausmannite whereas M3G1 shows a noteworthy decline of crystallinity indicating the high dispersion of Mn_3O_4 in the latter sample. M1G1 composite reveal appearance at $2\theta = 28.7°$ of new peak; correlated to the (110) plane, attributed to the α-MnO_2 phase [16,39]. M1G1 and M3G1 patterns shows another peak at $2\theta = 75°$ related to the (413) plane of Mn_3O_4; which are not detected in the pure forms of them. The crystallite sizes of M1G3, M1G1, M3G1 estimated by the Debye-Scherer formula were 23, 65 and 12 nm, respectively.

HR-TEM and SAED analyses were examined to determine the morphology of nanoparticle surfaces on the prepared composites compared to pure Mn_3O_4 (Fig. 2). Pure Mn_3O_4 reveals spherical nanoparticles with diameter average of 12 nm (Fig. 2a). The crystal structure of pure Mn_3O_4 was confirmed by the selected-area electron diffraction pattern (SAED) where it reveals strong rings related to (101), (103), (211) and (220) planes characteristic of the Hausmannite Mn_3O_4 phase. It was observed a well dispersion of these spherical nanoparticles with a slight aggregation creating clusters due to high surface energy of nanoparticles. M1G1 nanocomposite has nanoparticles with two different morphological shapes: spheres with an average diameter of 10 nm and squares with an average diameter of 44 nm dispersed on graphene nanosheets (Fig. 2b).

The selected area electron diffraction (SAED) pattern given in the inset Fig. 2b indicates the creation of the Hausmannite Mn_3O_4 phase owing to the existence of rings correlated to (101), (103) and (211) planes. Furthermore, the appearance of another diffraction ring characteristic of graphene's (002) plane suggests a strong bond between graphene nanosheets and Mn_3O_4. The TEM picture of the M3G1 nanocomposite (Fig. 2c) shows a variety of morphologies, including regular tetrahedrons, rectangular, and spherical structures with an average diameter of 10—12 nm. From exterior to interior, the SAED pattern specifies strong rings that correspond to (101), (103), (211), (220), and (002) planes that are associated with the Hausmannite Mn_3O_4 phase and graphene, respectively (002).
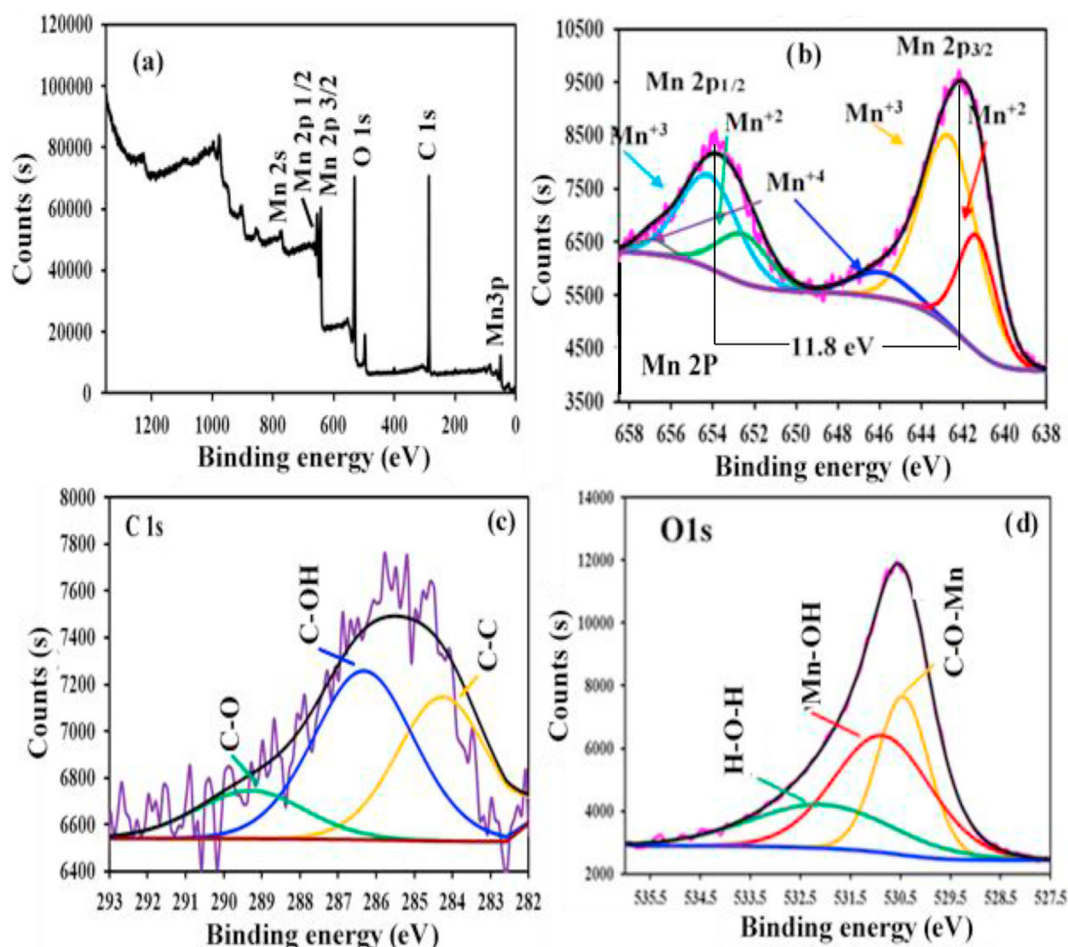

Fig. 3 — (a) Survey XPS spectrum of M3G1, (b) Mn 2p spectra of M3G1, (c) C 1s spectra of M3G1, (d) O 1s spectra of M3G1.

The significant interaction between graphene and Mn_3O_4 nanoarchitectures is confirmed by this pattern. The contact and distribution of Mn_3O_4 nanoparticles on graphene play an important role in preventing Mn_3O_4 nanoparticle aggregation, as evidenced by the alteration in shape after connection with graphene nanosheets. The small particle size enhances the interface surface area between graphene and Mn_3O_4 nanoparticles. On the other hand, the TEM images of M1G3 (Fig. 2d) reveal square and spherical nanoparticles with diameters of 50 nm and 12 nm, respectively.

4.2. X-ray photoelectron spectroscopy (XPS) study

The chemical composition of the Mn_3O_4/RGO nanocomposite was analyzed via X-ray photoelectron spectroscopy (XPS). Fig. 3 displayed the XPS of the Mn_3O_4/RGO nanocomposite. Clearly visible elements in the M_3G_1 XPS survey spectrum were Mn, O, and C. The energy gap between Mn 2p1/2 and the Mn mother sample is greater in the Mn 2p XPS spectrum, indicating a significant interaction with RGO. This energy gap difference between Mn 2p3/2 and Mn 2p1/2 was 11.8 eV, evidencing the exposure of Mn_3O_4. The Mn−O−C, Mn−OH, and the physisorbed or chemisorbed water bonds, respectively, are responsible for the decomposition of the high-resolution O1s spectra into three peaks at 529.82, 531.32, and 532.3 eV [40,41]. Three peaks at 284.4, 285.85, and 289.3 eV, which are attributed to C−C, C−OH, and C−O in rGO, respectively, deconstructed the high-resolution C1s spectra [42,43]. Consequently, the XPS results demonstrate that MnO−Mn_3O_4@rGO was prepared successfully.

4.3. FTIR and Raman spectroscopy

Fig. 4 represents the FTIR spectra of the obtained samples. It was observed that the spectrum of RG reveals small bands at 1039, 1112, 1383, 1415, 1581, 1632, and 1710 cm^{-1} approving the existence of remaining oxygen functional groups on its surface. Stretching vibrations of water-absorbed molecules and C=O were assigned via bands at 1632 cm^{-1} and 1710 cm^{-1}, respectively [19,44]. Whereas the bands at 1039, 1112, 1383 and 1415 cm^{-1} are indexed to C−OH and C−O stretching vibrations of the epoxy groups [35,36], carboxyl group bending vibration [45], and O−H bending vibrations of tertiary C−OH [46], respectively. The band at 1580 cm^{-1} is due to the aromatic C=C of unoxidized graphitic carbon that contribute to the reduction of GO [35,36,45]. Furthermore, the bands observed in the
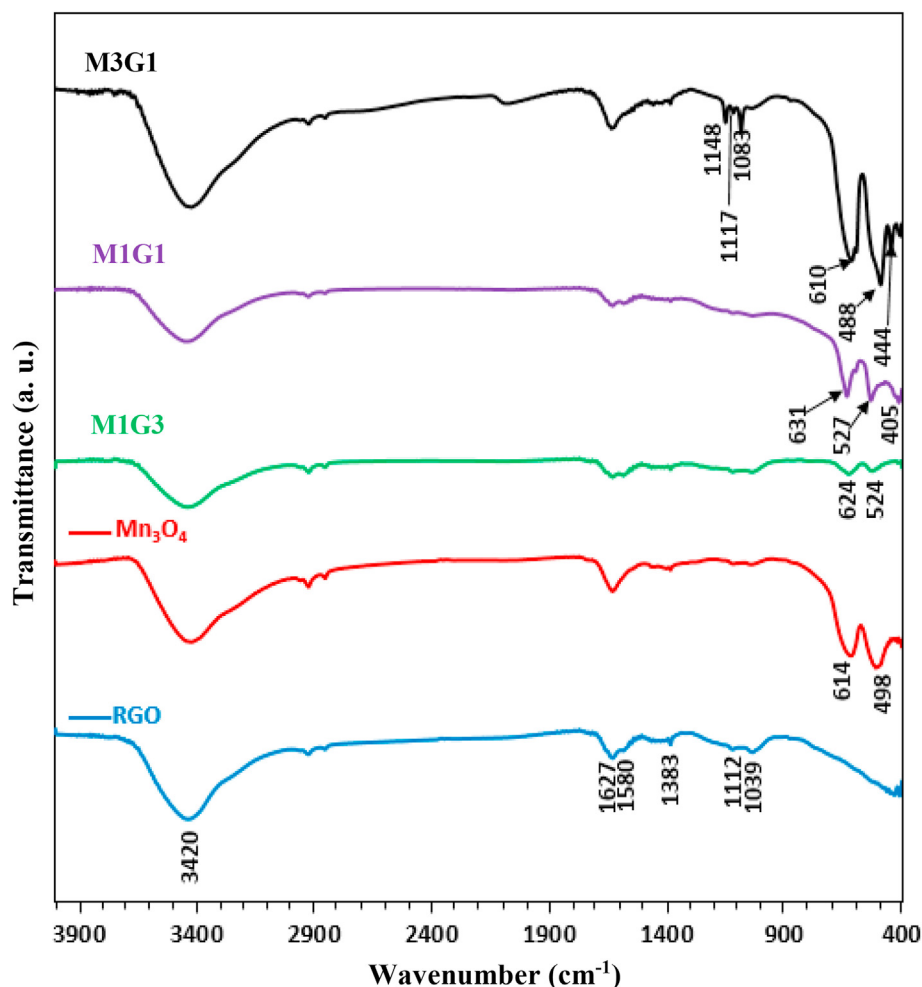

Fig. 4 — FTIR spectra of RGO, Mn_3O_4, M1G3, M1G1 and M3G1.

Mn_3O_4 spectrum at 1632 cm^{-1} assigned to water adsorbed, 1495 cm^{-1} due to OH deformation vibrations, and 1383, 1112 and 1039 cm^{-1} assigned to C−OH vibrations. These bands are suggestive of the notable presence of the acetate species. In addition, there are two bands at 614 and 498 cm^{-1} characteristics of Mn−O bending mode at tetrahedral sites and the distortion vibrations of Mn−O at octahedral sites, respectively. The M1G3 spectrum reveals the same band characteristics of both RG and Mn_3O_4 with a lower intensity for bands related to pure Mn_3O_4. This indicates the strong interaction and connection between graphene and Mn_3O_4. Furthermore, it was observed that there is redshift in the bands at 624 and 524 cm^{-1} related to Mn−O vibrations in the latter sample compared to the bands at 613 and 490 cm^{-1} for the pure Mn_3O_4, which reflects significantly the strong interaction revealed between Mn_3O_4 and GO. The ratio of the area of tetrahedral to that of octahedral bands in M1G3 is larger than in the pure, which exhibited the opposite tendency. The bands observed on M1G1 are similar to those observed on M1G3, with modest shifts in the bands appearing at 624 and 524 cm^{-1}; on M1G3, the bands appear at 631 and 527 cm^{-1}, respectively, with the evolution of a new, minuscule one at 405 cm^{-1}. The Mn−O vibrations of MnO_6 seen in α-MnO_2 species are more analogous to this band, supporting the M1G1 XRD results [47]. The M1G1 sample had the same intensity ratio for tetrahedral and octahedral band structures, which was unusual. It also displays that the band at 1627 cm^{-1} splits to offer a doublet in M1G1 and M1G3 samples, exposing a band at 1580 cm^{-1} in the process. Even with such high Mn_3O_4 loadings, this could

indicate a probable reduction in GO. The spectra of M3G1 composites with a high Mn_3O_4 to GO ratio, on the other hand, reveal bands at 610 and 488 cm^{-1}, as well as minor bands at 444 and 400 cm^{-1} attributable to Mn^{3+} in octahedral sites [48,49]. Raising the contents of Mn_3O_4 phase (M3G1) in comparison to other nanocomposites specifies the altered structure geometry of Mn_3O_4, and reduced strength with RGO. The emergence of bands at 1050-1400 cm^{-1} associated with the C−OH area, as well as a band at 3420 cm^{-1} due to OH stretching, with disappearance at 1580 cm^{-1} reflecting the oxidation action of Mn_3O_4 on RGO, at such high concentrations of Mn_3O_4. The existence of bands associated with MnO_2 in M1G1 and Mn_2O_3 in M3G1 could be attributed to thermodynamic surface energy fluctuations that permitted MnO_2 and Mn_2O_3 moieties to be exposed together with the most prominent Mn_3O_4 under wet conditions; this was substantially achieved under dry conditions [50,51]. This was validated by growing the width of the stretching of the O−H band as well as the C−OH stretching bands in M3G1. The disappearance in the XRD pattern of the Mn_2O_3 species of M3G1 reveals its modest amounts and actually improves the FTIR technique's sensitivity.

Raman spectra were tested to obtain more confirmation on the interaction and structure of the prepared composites. Raman spectra were measured for the GM nanocomposites compared to the Mn_2O_3 sample and given in Fig. 6. A prominent peak at 641 cm^{-1} in the Raman spectra of pure Mn_3O_4 is associated to the A_{1g} mode, which is indexed to the vibrations of oxygen in the MnO_6 unit [52]. The M1G1 Raman spectrum shows G and D peaks at 1570 cm^{-1} and 1347 cm^{-1}, respectively.
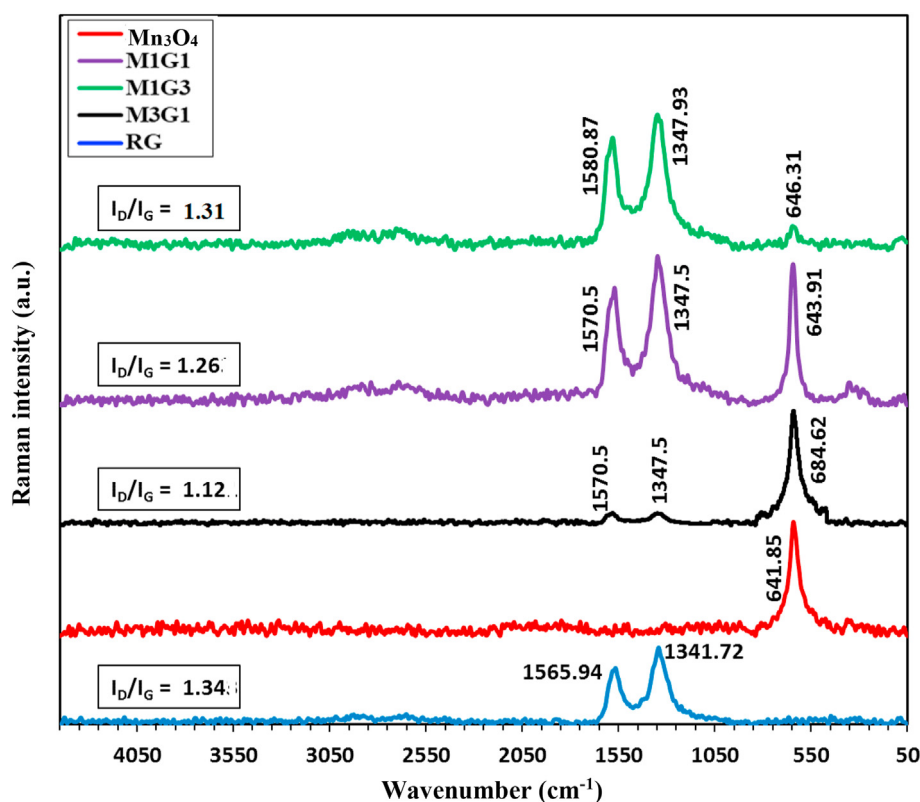

Fig. 5 – Raman spectra of RGO, Mn_3O_4, M1G3, M1G1 and M3G1.

The E_2g mode, which is connected with ordered sp2 bound carbon, is related to the G band. Disordered layers or edges are responsible for the D peak [53]. To better comprehend the reported weak contact among the GO and Mn_3O_4, the intensities of tiny peaks in the 200-400 cm^{-1} range attributed to Mn_3O_4 modes were raised in the M1G1 spectra compared to pure Mn_3O_4 [54]. The Mn_3O_4 mode was also retained in the composite M3G1 comparable to its free form except that it shows a marked decrease in intensity for D and G modes configured at 1347 and 1570 cm^{-1}, respectively. This could give an indication of the rigorous overlaying of Mn species on graphene surfaces. The M1G3 spectra, on the other hand, comprises D and G peaks as well as a very minor peak at

641 cm^{-1} ascribed to free Mn_3O_4 that is 0.2 of its strength in M1G1 and 0.25 of that in pure Mn_3O_4. The contact between graphene and Mn_3O_4 was stronger in M1G3 compared to the other nanocomposites, based on the Mn/GO ratio. Strong contact of graphene with Mn_3O_4 was achieved via shifting the G band from 1570 cm^{-1} in M1G1 and M3G1 to 1580 cm^{-1} in M1G3, as well as a reduction in the thickness of the graphene layers in this latter sample. The nanocomposites M1G1 and M1G3 display the 2D band extending from 2550 to 2850 cm^{-1} related to the two phonon lattice vibration with the same position and shape [55]. The crystallite size and disorder of the graphitic layers can be determined from the intensity ratio of D and G peaks (I_D/I_G). In comparison to M1G3 (1.31), M1G1
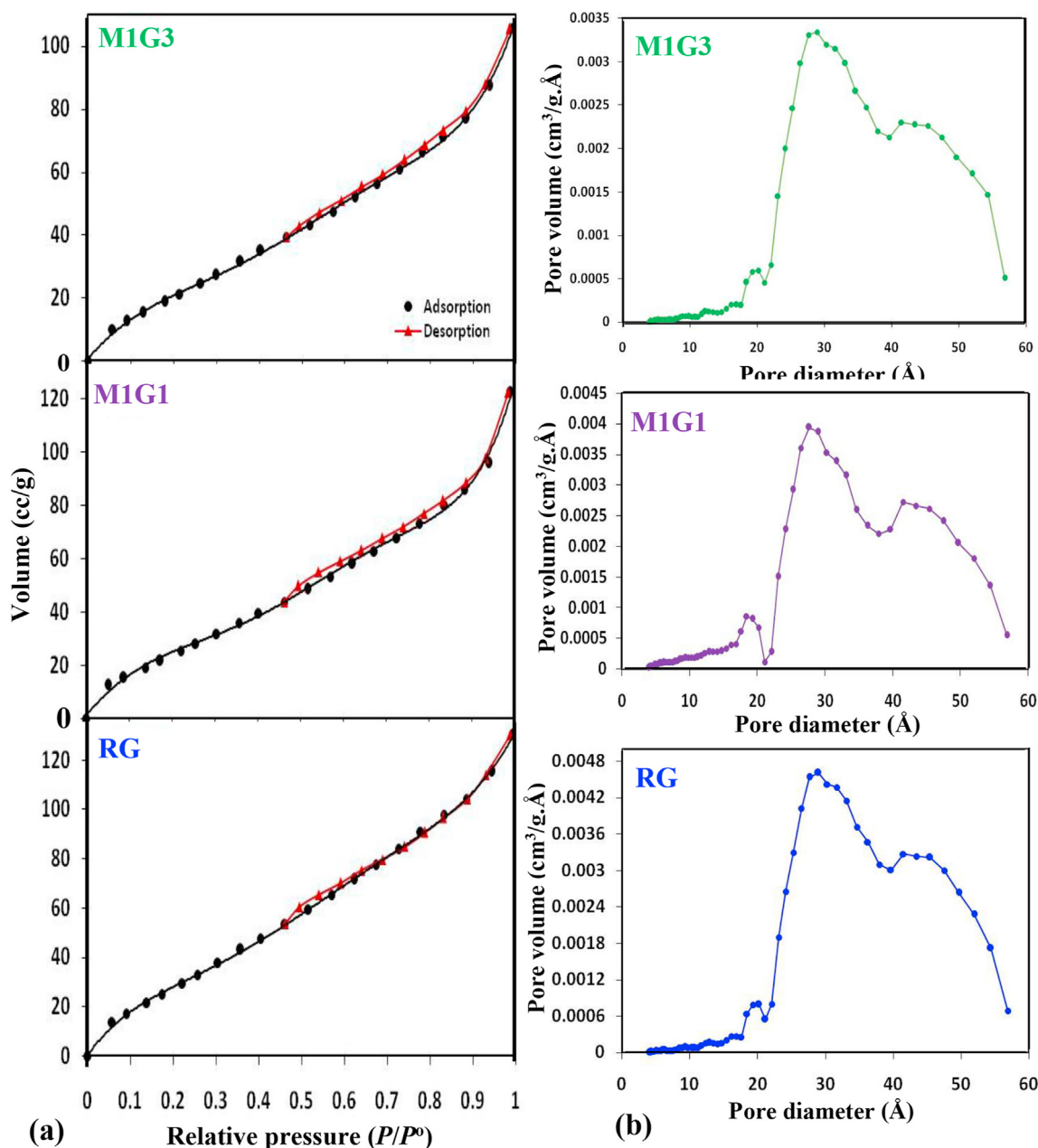

Fig. 6 − Adsorption-desorption isotherms of RGO, M1G3 and M1G1 samples (a), together with their corresponding pore size distributions (b).

(1.26), and M3G1 (1.12), RG exhibits a high I_D/I_G intensity ratio of (1.34), indicating a reduced density of imperfection in RG after Mn_3O_4 insertion. However, this ratio is not straightforward in the M3G1 sample that showed great diminishing in D and G bands intensities. This may not involve the disruption of graphene ordering but is presumably correlated to the presence of plenty of Mn_3O_4 groups between graphene sheets, masking the proper appearance of both D and G bands.

4.4. Surface texturing

Fig. 6a displays the N_2 adsorption-desorption isotherms of some of the nanocomposites that were prepared, as well as their PSD curves (Fig. 5b). They revealed an isotherm of type IV with hysteresis loop H3 representing slit-shaped or plate-like pore aggregation [56]. After mixing Mn_3O_4 with RG, the surface area (S_{BET}) declined from 142.6 m^2 g^{-1} in pure RG to 116 m^2 g^{-1} in M1G1, 130 m^2 g^{-1} in M3G1, and 105.6 m^2 g^{-1} in M1G3. It was revealed that the hysteresis loops of RG close at P/P^o value of 0.46, M3G1 close at 10.46, and M1G3 close at 10.45. This implies that all of the samples have similar big pores, with the exception of RG, which has an extra hysteresis loop at P/P^o = 0.84, suggesting the envelopment of mesopores. After the addition of Mn_3O_4, the hysteresis vanishes, suggesting that the latter is fully inserted between the RG sheets. It was found that the pore volume values of RG (0.1124 cm^3 g^{-1}), M3G1 (0.0941 cm^3 g^{-1}), M1G1 (0.0912 cm^3 g^{-1}), and M1G3 (0.0818 cm^3 g^{-1}) followed the similar tendency as their surface area values. These results explain a narrowing of the pore radius only for M1G1 (27.67 Å) and M3G1 (26.3 Å) samples and it was reluctant in M1G3 (28.9 Å), which was typical to the value of RG, which leads to a reduction in pore volume of composites. The presence of three types of pores (4.3 nm, 2.8 nm, and 2.1 nm) in the mesopores of low range can be seen in the curves of the distribution of pore size (PSD) of all samples. M1G3>M1G1>RG was the sequence in which the relative intensity of the peaks connected to distinct kinds of pores decreased. This explains why Mn_3O_4 is inserted well among RG sheets in M1G3 and M1G1 samples, resulting in a sturdy contact between the moieties. Furthermore, lowering the pore radius of M3G1 without significantly changing the pore volume reveals that the majority of Mn species are close to the surface. The M1G3 sample, on the other hand, had the smallest pore volume compared to the other samples while maintaining the same pore radius, which suggests Mn_3O_4 dispersion deep within the RG pores.

4.5. Supercapacitive characteristics

The capacitive behavior of electrode materials can be studied using cyclic voltammetry (CV). In comparison to pure Mn_3O_4, Fig. 7 depicts CV curves of Mn_3O_4 integrated graphenes recorded in the potential window of $-0.85 - 0.65$ V, performed in 1.0 M Na_2SO_4, and at a scan rate of 50 mVs^{-1} (inset Fig. 7). All of the CV curves have a pair of redox peaks that correspond to the reversible $Mn^{2+} \leftrightarrow Mn^{3+}$ reactions [25,57]. The redox reaction peaks on the rectangular and asymmetric CV curves imply a combination of electric double-layer capacitances from rGO and Faradic pseudocapacitive behavior from Mn_3O_4. The specific capacitance C_{sp} of the investigated electrodes was estimated using the CV curves and the equation below [57,58].
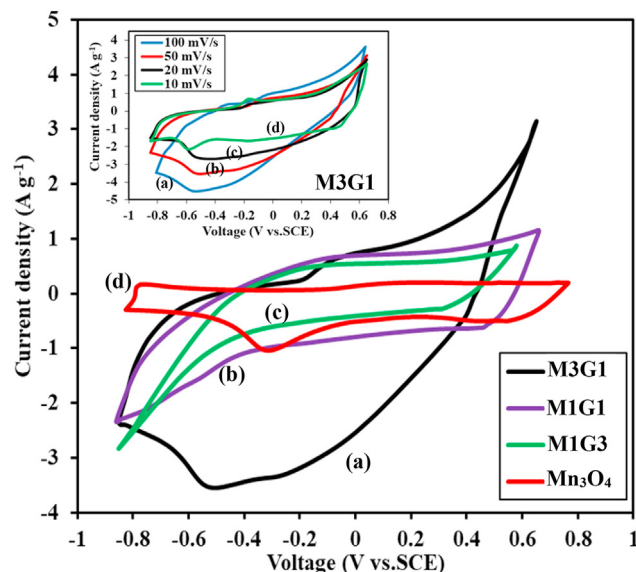

Fig. 7 – The CV curves of a) M3G1, b) M1G1, c) M1G3 and d) Mn_3O_4 electrodes measured in the potential window of -0.85:0.65 V; performed in 1.0 M Na_2SO_4, and at scan rate of 50 mVs^{-1}. Inset Fig. relates the corresponding CV curves of M3G1 at the scan rates of a) 100 mV/s, b) 50 mV/s, c) 20 mV/s and d) 10 mV/s in 1.0 M Na_2SO_4.

$$Csp = \frac{1}{vw(\Delta V)} \int_{Va}^{Vc} iVdV \qquad (1)$$

Where ΔV (V) is the potential drop, v (mV s^{-1}) is the scan rate, and w (g) is the active material mass. The results are presented in Table 1. When compared to pure Mn_3O_4 and other composite samples, the results demonstrate that M1G3 has the highest specific capacitance. At a scan rate of 50 mV s^{-1}, the specific capacitance values of Mn_3O_4, M1G1, M1G3, and M3G1 are 45, 77, 40, and 148 F g^{-1}, respectively. The beneficial synergistic effects between graphene and Mn_3O_4 may explain the capacitive performance of the Mn_3O_4/graphene composite electrode. As seen in SEM photos, graphene in composite samples serves as a 2D support material that uniformly anchors or disperses the micro Mn_3O_4 particles. At the same time, incorporating Mn_3O_4 particles into graphene can prevent graphene sheets from stacking and agglomerating, making them accessible to electrical and ionic transport channels. Furthermore, graphene provides a highly conductive net for electron transport throughout the charge and discharge courses, overcoming the pure Mn_3O_4's poor electrical characteristics and charge transfer pathways.

Table 1 – Specific capacitance values of synthesized samples at different scan rates.

Scan rate (mVs^{-1})	Specific capacitance C$_{sp}$ (F g^{-1})			
	Mn_3O_4	M3G1	M1G1	M1G3
100	25	88	51	32
50	45	148	77	40
20	56	332	104	64
10	-	440	134	87

Under the same experimental condition, our specific capacitance value of Mn_3O_4 is higher than that found by porous nanostructured Mn_3O_4 synthesized by a hydrothermal method using the CTAB surfactant (22.5 F g^{-1}) [59]. Our value also exceeded different Mn_3O_4 architectures or CNT-supported Mn_3O_4 composites reported recently [60,61]. Among the nanocomposites, M3G1 showed the highest current density and CV area and thus the highest specific capacitance value. Indeed, the open pore design and size distribution observed in M3G1 together with high S_{BET}, as determined by N_2 sorptiometry measurements, dictate easy ion transport and thus increased ionic conductivity. Undeniably, the expected rapid transformation between Mn^{3+} and Mn^{2+} moieties as well as the residual oxygen moieties; those intrinsically controlled partially oxidized graphene sheets, affected markedly the performance of this sample and indeed increases the conductivity and the pseudocapacitance behavior. Conversely, lowering the Mn_3O_4 active sites (as in M1G3) will announce the restacking of graphene nanosheets and thus restrict the electron/ion transfer processes in a facile way.

CV characterizations were accomplished at sweep rates of 100, 50, 20, and 10 mV s^{-1} to obtain more information on the electrochemical behavior of the M3G1 electrode (greater capacitance electrode) (inset in Fig. 7). As a result, the CV curves produced exhibit essentially no significant change when the scan rates increase. This refers to the electrode's excellent electron conduction and low equivalent series resistance. Furthermore, as the scan rate is increased, the specific capacitance decreases, giving a C_{sp} value of 440 at 10 mV s^{-1}, indicating good rate property and an outstanding capacitance trend. The behaviour of the M1G3 CV curve was comparable to the one devoted for M3G1 and Mn_3O_4 (not shown). This highlights that the ion transport is not amenable to diffusing into the electrode/electrolyte interface with increasing scan rates in the electrode samples. Because of the time constraint, the diffusion of electrolyte ions is limited at high scan rates.

It is significant notifying that the specific capacitance of the as-synthesized M3G1 (at 10 mV s^{-1}, C_{sp} = 440 F g^{-1}) composite exceeds that of Mn_3O_4/graphene nanocomposites in 1.0 M Na_2SO_4 electrolyte 130 F g^{-1}) as well as Mn_3O_4/graphene prepared via ethylene glycol route (at 5 mV s^{-1}, C_{sp} = 159 F g^{-1}) [31,62]. Also, it exceeds the value supplied from GO/Mn_3O_4 thin films synthesized using a successive ionic layer adsorption (344 F g^{-1}) [31].

GCD measurements were used to study the electrode materials' electrochemical characteristics. At 250 mA/g current density, Fig. 8 depicts potential vs. time curves for pristine Mn_3O_4 (inset) and Mn_3O_4/graphene nanocomposites. The faradaic response (Pseudocapacitance) is related to the deviation (distorted) observed in the charge-discharge curves, which is compatible with the stated CV curves [62,63]. From the discharge cycles, the below relation was used to estimate the specific capacitances of the investigated electrodes [4,5]:

$$C_{sp} = It/mV \qquad (2)$$

Where I, t, m, and V represent the current loading, the discharge time, the mass of the active material in working electrode, and the potential window, respectively [58,62,64]. It was found that the specific capacitances of the M3G1, M1G1,
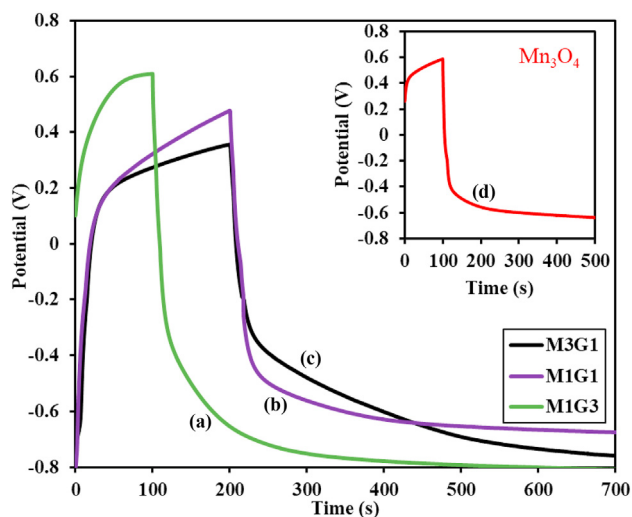

Fig. 8 – The potential vs. time curves for a) M1G3, b) M1G1, c) M3G1 nanocomposites and d) Mn_3O_4 (inset) performed in 1.0 M Na_2SO_4 at a current density 0.25 A/g.

M1G3 and Mn_3O_4 electrodes are 490, 416, 333, and 187 F g^{-1} at 250 mA g^{-1}, respectively (Table 2). The values obtained refer to the M3G1 sample having the highest capacitance, which is consistent with those found by CV measurements. When using a supercapacitor in a power application, rate capability is critical. As a result, we analyzed the charge/discharge behavior of the electrodes under investigation at various current densities (25–100 mA g^{-1}). The specific capacitance values indicate diminution behaviour in the following order: M3G1> M1G1> M1G3> Mn_3O_4 (Table 2). Indeed, decreasing the capacitance values while increasing the current density confirms the aforementioned CVs results, in which an increase in capacitance was achieved as a decrease in scan rate. The IR_{int} decline of the charge-discharge curves decreases with increasing the charging currents for all the samples (Table S1) from 0.25 to 1.0 mAg^{-1}.

Table 3 summarizes the specific capacitance of Mn_3O_4/Graphene composites compared with other composites. M3G1 nanocomposite shows higher capacitance values than previously reported values for other Mn_3O_4/G composites [62,63,65–72].

Because life cycle is such a critical factor in applications of supercapacitor, a life cycling test was performed for the investigated electrodes using the galvanostatic charge–discharge technique at a constant current density of 0.25 A g^{-1} for 1000 cycles in the potential range of –0.85 to 0.65 V. The results

Table 2 – Specific capacitance values of synthesized samples at different current densities.

Current density (A g^{-1})	C_{sp} Specific capacitance (F g^{-1})			
	Mn_3O_4	M3G1	M1G1	M1G3
0.25	187	490	416	333
0.5	142	325	196	154
1	129	226	153	128

Table 3 — Summary of electrochemical performance reported in literature for Mn₃O₄/Graphene composites as a supercapacitor electrode material.

System	Synthesis method	Electrolyte, current collector	capacitance retention	Specific capacitance C_s (F/g)	Ref.
GM composite	one-step solvothermal process	1.0 M Na_2SO_4, stainless foil	88% after 500 cycles	130 ($i = 1$ A/g)	[62]
GM composite	precipitation from MnO_2 organosol	Na_2SO_4, platinum foil	-	175 ($v = 5$ mV/s)	[63]
GO/Mn_3O_4	facile low temperature solid reaction method	1 M Na_2SO_4, glass/stainless steel substrate	87% over 3000 cycles	300 ($v = 10$ mV/s)	[65]
$Graphene/Mn_3O_4$	simple and environmentally friendly chemical process	0.5 M NaCl, nickel foam	87% over 2000 cycles	239.6 ($v = 10$ mV/s)	[66]
GMn80	microwave-assisted hydrothermal synthesis	0.5 M Na_2SO_4	—	193 ($v = 25$ mV/s)	[67]
1-GM composite	Polyol process along with annealing	stainless steel	91% after 1500 cycles	293 ($v = 5$ mV/s), 230.4 ($i = 1$ A/g)	[68]
GM composite	hydrothermal self-assembly	1 M Na_2SO_4, Carbon flake		148 ($i = 1$ A/g) F/g	[69]
Nitrogen-doped graphene—Mn_3O_4 nanohybrids	hydrothermal	0.5 M Na_2SO_4 + 5 mM $NaHCO_3$, nickel foam		206 ($i = 1$ A/g)	[70]
RGM-0.5	chemical decomposition	1 M Na_2SO_4, Stainless steel mesh		131 ($i = 0.5$ A/g)	[71]
GM composite	hydrothermal	Na_2SO_4 solution, nickel foam,	100% after 10,000 cycles	114 ($v = 5$ mV/s), 121 ($i = 0.5$ A/g)	[72]
M3G1	deposition-solvothermal process	1.0 M of Na_2SO_4, FTO conductive glass	100% after 10,000 cycles	440 ($v = 10$ mV/s), 226 ($i = 1$ A/g)	This work

obtained are shown in Fig. 9. The variation in the capacitance retention as a function of the cycle number for M3G1 was consistent during the 1000 cycles giving ~100% retention. Whereas, for M1G3 a continuous decrease in the specific capacitance with retention equal to 82% was perceived at the end of the 1000 cycles. On line, the M1G1 electrode exhibits a decrease during the first 760 cycles retaining a 92% capacitance value that goes up afterward, reaching 98% at the end of the 1000 cycle. The Mn_3O_4 electrode exhibits a stability for the first 140 cycles (giving 100%) followed by a narrow decrease reaching
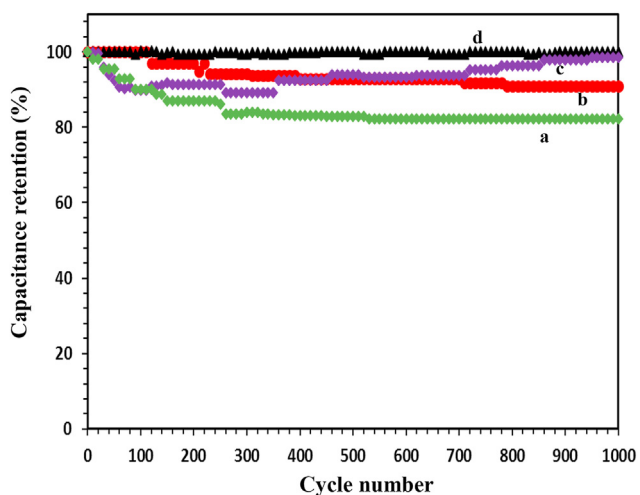
93% after completing the 1000 cycles, contrasting other types of Mn_3O_4 those used to present marked diminish in the capacitance in 400—1000 cycles [25,73,74]. This exceptional performance and the high rate capability do indeed depend on the synergism between Mn_3O_4 and graphene as well as their proportions. As a result, the M3G1 electrode's stability over capacitance retention cycles may be connected to the connections between the moieties that make up the electrode, even though it's not quite high as compared to other nanocomposites but was enough to assist electronic and ionic transitions from active sites into the charge collectors. Particularly, exposing Mn_3O_4 close to the surface; as established via the surface texturing results is expected to reduce the charges diffusion paths within the electrode surface that indeed maximized via the exhibited high surface area and decreased crystallites sizes. Definitely, the latter characteristics enhanced the active sites; compared to other nanocomposites, in which rapid charge transitions are exhibited and improved via the 3D network polyhedral structure of Mn_3O_4. That designed 3D structure has a large number of accumulated active sites as well as a high porosity capable of tailoring mass transport [72].

Despite M1G1 presenting other species other than Mn_3O_4 as M3G1 did, such as MnO_2, it presented lower capacitance and stability due to decreasing surface area as well as increasing the crystallite size. This could also give a hint about phase change and the possibility of inducing side reactions in active materials and thus instability [74]. The dielectric constants of M1G1 and M1G3 samples were expected to exceed those of M3G1 based on increasing the graphene ratio, a well-known high conductivity value. However, their decreased supercapacitor values are probably due to the fact that the heterojunction formed between the moieties of the former

Fig. 9 — The galvanostatic charge—discharge curves at a constant current density of 0.25 A g^{-1} in the potential range from −0.85 to 0.65 for 1000 cycles for a) M1G3, b) Mn_3O_4, c) M1G1 and d) M3G1 samples.

samples was not as strong as in the latter, i.e., the CV and V-t curves approved the action of M3G1. The presence of residual oxygens on graphene surfaces of M3G1 was found to be effective in imparting electrostatic interactions (RG-O-Mn) that prevented restacking and thus facilitated electron-proton transitions. Nevertheless, the presence of individual graphene sheets in M1G1 and M1G3; as exhibited in TEM images, makes the graphene electrode is inaccessible due to restacking via the strong $\pi-\pi$ interaction and the consequences thereof concerning the delay of electron transition. The rate capability of super-capacitors is critical for their use in power applications. To supply high energy density at a high charge/discharge rate, an appropriate electrochemical energy storage technology is required. Because the power density (P, W kg^{-1}) and energy density (E, Wh kg^{-1}) are two critical parameters in practical applications, the Ragone plots of Mn_3O_4 and its nanocomposites with RGO were analyzed using the equations below [8,9,15,75,76]:

$$E = 0.5 \, C_{SP} \, (\Delta V)^2 \qquad (3)$$

$$P = E/t \qquad (4)$$

Where C_{sp}, ΔV, and t represent the specific capacitance of the supercapacitor (F g^{-1}), the voltage changes after the IR drop in V during the discharge process, and the time for a sweep segment (h). The estimated values of E and P are represented in Fig. 10, as Ragone plots (E vs. P). Mn_3O_4 reveals an energy density of 12.5 Wh Kg^{-1} at a power density equal to 998 W kg^{-1} and maintains the lowest energy density of 6 Wh Kg^{-1} at the highest power density of 3096 W kg^{-1}. Such a line plateau is a feature of redox processes of the Mn_3O_4 moieties. Albeit, M1G1 indicates an energy density comprises of 33 Wh Kg^{-1} with power density equal 618 W kg^{-1}, it shows a great decrease with scan speed into 18 Wh Kg^{-1} at an enormously high power density of 2713 W kg^{-1}. An equivalent behaviour to the latter samples was also depicted for the M1G3 sample via visualizing an energy density as high as 28 Wh Kg^{-1} at a power density of 232 W kg^{-1} and maintaining 8 Wh Kg^{-1} at a high power density of 2489 W kg^{-1}. Increasing the propensity of the specific power
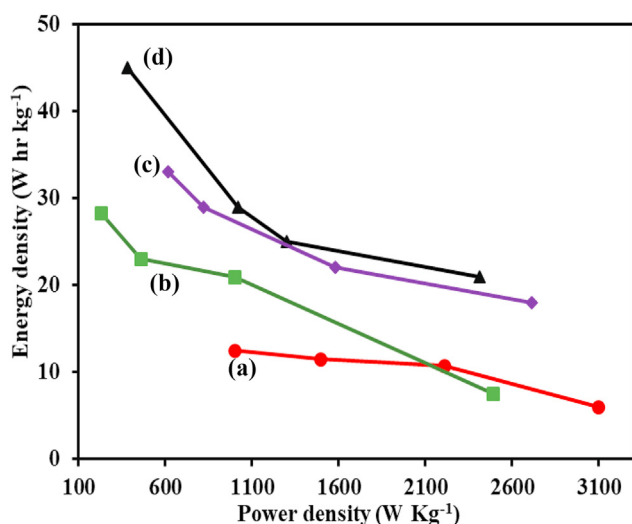
of our nanocomposites discloses that the discharging capacity of such supercapacitors is directly proportional to the discharging current. Whereas, the decreasing behavior of the specific energy recommends that parts of the electrode surfaces are even attainable at high charging-discharging current. It's clarified that the nanocomposite M3G1 indicates a high-quality electrochemical reversibility and signifies the highest energy, superior stability and highest specific capacitance value of 490 F g^{-1}. The electrochemical properties of the studied samples were further assessed with electrochemical impedance spectroscopy (EIS). The EIS were examined to not only affirm the above results obtained via CVs and charge-discharges but also to acquire information concerning the facile transport of ions and electrons and their conductivities. The EIS was performed at an open potential over the frequency margin of 0.1−140 Hz with an amplitude equal to 5 mV (Fig. 11).

The Nyquist plots indicate precise semicircles at high frequencies for all nanocomposites and linear parts at low frequencies. The charge transfer resistance of the electrode, which is related to the faradaic redox process in the system, causes the semicircular loop at high frequencies. The diameter of this semicircle can be used to determine the charge-transfer resistances Rct. R_{ct} was found to decrease in the order: M3G1<M1G1<M1G3< Mn_3O_4. On the contrary, the slope of the straight line was much steeper in the order: M3G1 > M1G1 > M1G3> Mn_3O_4 indicating that M3G1 has the least interfacial charge-transfer resistance and lowest diffusion resistances and thus revealed the highest specific capacitance, compared to the rest of the nanocomposites.

Bode plots (not shown) are further confirmed EIS analyses via illustrating that the change in the frequency peak position related to the charge transfer at the M3G1 electrode was the lowest comprehending longer charges lifetime, comparatively. An equivalent circuit is provided from the electrochemical impedance (EIS) of the nanocomposites data that

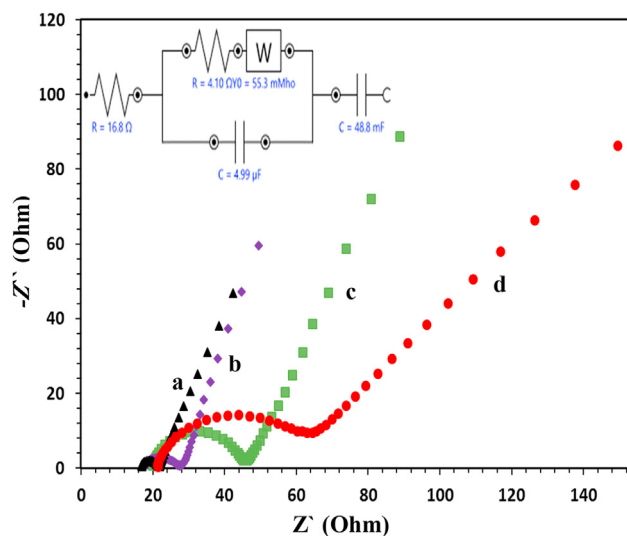Fig. 10 − Ragone plots of a) Mn_3O_4, b) M1G3, c) M1G1 and d) M3G1 samples.

Fig. 11 − Electrochemical impedance spectra of a) M3G1, b) M1G1, c) M1G3 and d) Mn_3O_4 samples, performed at an open potential in the frequency margin of 0.1−140 Hz with an amplitude equal 5 mV, and the inset is the M3G1 circuit.

Table 4 – The values of R_s, R_{ct} and the time constant for pure Mn_3O_4 and its nanocomposites with RGO.

Sample	τ (s) [$\times 10^{-4}$]	R_s (Ω)	R_{ct} (Ω)
Mn_3O_4	3.38	21	47
M3G1	0.201	17	5
M1G1	0.354	18	10
M1G3	1.093	20	25

includes a resistance of bulk solution (Rs), a resistance of charge-transfer (Rct), an element of pseudocapacitive (C) from the Mn_3O_4/GO redox process, and resistance of Warburg (W) due to diffusion of ions. As seen in the inset of Fig. 10, this was in parallel with another element Cdl of the double layer capacitance. This M3G1 inset circuit demonstrates the circuit's close resemblance to the original data gathered from CVs and charge-discharge phenomena, as well as the concurrence of the pseudocapacitive and double layer capacitance. Using the following equation, $\tau = 1/2\pi f_{max}$. the time constant of the capacitor (τ, s) may be evaluated from the frequency (f_{max}, Hz) commensurate with the maximum of

Fig. 12 – TEM Images of the electrodes after 1000 cycle M3G1 and M1G3.

imaginary impedance (Z″) of the semicircle in the impedance spectra [77,78]. The time constants with other impedance parameters are given in Table 3. The time constant was found to be the lowest for M3G1 in comparison to the other materials. The M3G1 electrode took the least time to charge the capacitor. In comparison to Mn_3O_4 electrode, the other parameters mentioned in Table 4 clearly illustrate that the hybrid composite electrodes allow simpler access (reduced resistance) for charge intercalation and deintercalation via elaborating R_s, R_{ct} and the time constant values.

The good fit between the simulated and experimental data was established by mathematical modelling of generated impedance spectra (using software by Boukamp [79]). The average error of regression, denoted by χ2, was used to describe the fit quality [79,80]. The proposed circuit given in Fig. 11 is similar for all samples with χ^2 values of 0.0396, 0.0552 and 0.632 for samples M3G1, M1G1 and M1G3, respectively.

After the stability test, we also carried out TEM study, as shown in Fig. 12. It appears that no substantial alterations are displayed for the M3G1 sample, with the exception of a few alterations concerning the size increase from 12 nm to 20 nm; however, it is still in contact with the graphene moieties. The consistency of the electrode was unaffected by such changes. Similar to the M3G1, the M1G3 did not show any significant alterations, although its reduced activity is primarily due to charge transfer resistance and its longer path. In addition, surface texturing metrics like pore volume, radius, and surface area were far lower than in the M3G1 sample.
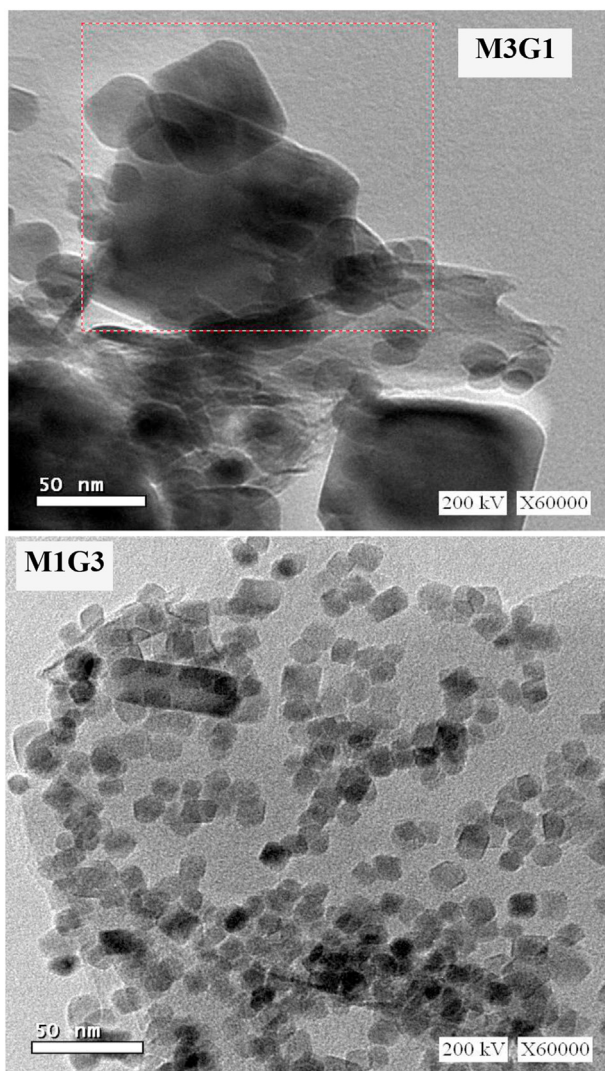
5. Conclusion

The adoption of deposition–solvothermal technique for synthesizing RG-Mn_3O_4 nanocomposites has stimulated the innovation of supercapacitors of unprecedented performances and at most the nanocomposite M3G1 has exhibited a C_{sp} value of 490 F g^{-1} at current density 0.25 A g^{-1}. This remarkable performance is attributed to the unique 3D Mn_3O_4 array that cooperated in increasing the electrode surface area as well as facilitating electrolyte access due to its hybridization with graphene sheets. This indeed has a high impact on shortening the electron/ion diffusion processes in the active materials. It seems that reduced graphene oxide moieties (oxygen content ratio) played a unique role in enhancing the ionic diffusion coefficient in M3G1 unlike other nanocomposites that suffer the shielding effect of the reduced graphene. M3G1 has shown the property of the pseudocapacitance and achieved high-energy density, high-power density, and long-term life for supercapacitor electrode applications. Increasing the disordering in M1G1 and M1G3 was one of the factors that seriously affected the electric diffusion and thus their specific capacitance values.

Declaration of Competing Interest

The authors declare that they have no known competing financial interests or personal relationships that could have appeared to influence the work reported in this paper.

Appendix A. Supplementary data

REFERENCES

[1] Akbar MZ, Bahareh A, Saied SHD. Fabrication of hollow $MnFe_2O_4$ nanocubes assembled by CoS_2 nanosheets for hybrid supercapacitors. Chem Eng J 2022;435:135170.

[2] Bahareh A, Akbar MZ, Saied SHD. Engineering of hierarchical $NiCoSe_2$@NiMn-LDH core-shell nanostructures as a high-performance positive electrode material for hybrid supercapacitors. Sustain Energy Fuels 2020;4:5144—55.

[3] Akbar MZ, Saied SHD, Mona MA, Morteza S. Designing an asymmetric device based on graphene wrapped yolk—double shell $NiGa_2S_4$ hollow microspheres and graphene wrapped FeS_2—$FeSe_2$ core—shell cratered spheres with outstanding energy density. J Mater Chem 2019;7:10282—92.

[4] Akbar MZ, Saied SHD. Construction of complex copper-cobalt selenide hollow structures as an attractive battery-type electrode material for hybrid supercapacitors. Chem Eng J 2020;402:126241.

[5] Bahareh A, Akbar MZ, Saied SHD. An advanced hybrid supercapacitor constructed from rugby-ball-like $NiCo_2Se_4$ yolk—shell nanostructures. Mater Chem Front 2021;5:4725—38.

[6] Liu TC, Pell WG, Conway BE. Self-discharge and potential recovery phenomena at thermally and electrochemically prepared RuO_2 supercapacitor electrodes. Electrochim Acta 1997;42:3541—52.

[7] Zhao X, Sánchez BM, Dobson PJ, Grant PS. The role of nanomaterials in redox-based supercapacitors for next generation energy storage devices. Nanoscale 2011;3:839—55.

[8] Akbar MZ, Bahareh A, Saied SHD. A high-energy-density supercapacitor with multi-shelled nickel—manganese selenide hollow spheres as cathode and double-shell nickel—iron selenide hollow spheres as anode electrodes. Nanoscale 2021;13:2931—45.

[9] Akbar MZ, Bahareh A, Saied SHD. α-MnS@Co_3S_4 hollow nanospheres assembled from nanosheets for hybrid supercapacitors. Chem Eng J 2021;422:129953.

[10] Karthikeyan K, Parthiban P, Vimal KM, Swapnil SN, Surjit S, Sang-Jae K. Probing the energy conversion process in piezoelectric-driven electrochemical self-charging supercapacitor power cell using piezoelectrochemical spectroscopy. Nat Commun 2020;11:2351.

[11] Yafei L, Xuming D, Yi L, Enhui B, Xianglin R, Huiyu C, Xiaodong T, Chunju X. Nanosheet-assembled porous MnCo2O4.5 microflowers as electrode material for hybrid supercapacitors and lithium-ion batteries. J Colloid Interface Sci 2022;627:815—26.

[12] Jiale S, Xuming D, Runze W, Yanfei Z, Chunju X, Huiyu C. Bundlelike $CuCo_2O_4$ microstructures assembled with ultrathin nanosheets as battery-type electrode materials for high-performance hybrid supercapacitors. ACS Appl Energy Mater 2020;3(8):8026—37.

[13] Runze W, Jiale S, Chunju X, Huiyu C. $MgCo_2O_4$-based electrode materials for electrochemical energy storage and conversion: a comprehensive review. Sustain Energy Fuels 2021;5:4807—29.

[14] Wei WF, Cui XW, Chen WX, Ivey DG. Manganese oxide-based materials as electrochemical supercapacitor electrodes. Chem Soc Rev 2011;40:1697—721.

[15] Hu CC, Wu YT, Chang KH. Low-temperature hydrothermal synthesis of Mn_3O_4 and MnOOH single crystals: determinant influence of oxidants. Chem Mater 2008;20:2890—4.

[16] Cottineau T, Toupin M, Delahaye T, Brousse T, Belanger D. Nanostructured transition metal oxides for aqueous hybrid electrochemical supercapacitors. Appl Phys A 2006;82:599—606.

[17] Goٖmez H, Ram MK, Alvi F, Villalba P, Stefanakos E, Kumar A. Graphene-conducting polymer nanocomposite as novel electrode for supercapacitors. J Power Sources 2011;196:4102—8.

[18] Oliveira HP, Sydlik SA, Swager TM. Supercapacitors from free-standing polypyrrole/graphene nanocomposites. J Phys Chem C 2013;117:10270—6.

[19] Wu NL, Wang SY, Han CY, Wu DS, Shiue LR. Electrochemical capacitor of magnetite in aqueous electrolytes. J Power Sources 2003;113:173—8.

[20] Durmus Z, Baykal A, Kavas H, Direkci M, Toprak MS. Ovalbumin mediated synthesis of Mn_3O_4. Polyhedron 2009;28:2119—22.

[21] Davar F, Salavati-Niasari M, Mir N, Saberyan K, Monemzadeh M, Ahmadi E. Thermal decomposition route for synthesis of Mn_3O_4 nanoparticles in presence of a novel precursor. Polyhedron 2010;29:1747—53.

[22] (a). Mehdizadeh R, Saghatforoush LA, Sanati S. Solvothermal synthesis and characterization of α-Fe_2O_3 nanodiscs and Mn_3O_4 nanoparticles with 1,10-phenanthroline. Superlattice Microst 2012;52:92—8.

(b). Song M, Cheng S, Chen H, Qin W, Nam K, Xu S, Yang X, Bongiorno A, Lee J, Bai J, Tyson TA, Cho J, Liu M. Hierarchically nanostructured carbon-supported manganese oxide for high-performance pseudo-capacitors. Nano Lett 2012;12:3483—90.

[23] Fang M, Tan XL, Liu M, Kang SH, Hu XY, Zhang LD. Low temperature synthesis of Mn_3O_4 hollow-tetrakaidecahedrons and their application in electrochemical capacitors. CrystEngComm 2011;13:4915—20.

[24] Jiang H, Zhao T, Yan CY, Ma J, Li CZ. Hydrothermal synthesis of novel Mn_3O_4 nano-octahedrons with enhanced supercapacitors performances. Nanoscale 2010;2:2195—8.

[25] An GM, Yu P, Xiao MJ, Liu ZM, Miao ZJ, Ding KL, Mao LQ. Low-temperature synthesis of Mn_3O_4 nanoparticles loaded on multi-walled carbon nanotubes and their application in electrochemical capacitors. Nanotechnol 2008;19:275709—15.

[26] Zhou TX, Mo SS, Zhou SL, Zou WJ, Liu YL, Yuan DS. Mn_3O_4/Worm-Like mesoporous carbon synthesized via a microwave method for supercapacitors. J Mater Sci 2011;46:3337—42.

[27] Cui XW, Hu FP, Wei WF, Chen WX. Dense and long carbon nanotube Arrays decorated with Mn_3O_4 nanoparticles for electrodes of electrochemical supercapacitors. Carbon 2011;49:1225—34.

[28] Novoselov KS, Geim AK, Morozov SV, Jiang D, Zhang Y, Dubonos SV, Grigorieva IV, Firsov AA. Electric field effect in atomically thin carbon films. Science 2004;306:666—9.

[29] Dikin DA, Stankovich S, Zimney EJ, Piner RD, Dommett GHB, Evmenenko G, Nguyen ST, Ruoff RS. Preparation and characterization of graphene oxide paper. Nature 2007;448:457—60.

[30] Lee JW, Hall AS, Kim JD, Mallouk TE. A facile and template-free hydrothermal synthesis of Mn_3O_4 nanorods on graphene sheets for supercapacitor electrodes with long cycle stability. Chem Mater 2012;24:1158—64.

[31] Wang B, Park J, Wang C, Ahn H, Wang G. Mn_3O_4 nanoparticles embedded into graphene nanosheets: preparation, characterization, and electrochemical properties for supercapacitors. Electrochim Acta 2010;55:6812—7.

[32] Li L, Hu Z, Yang Y, Liang P, Lu A, Xu H, Hu Y, Wu H. Hydrothermal self-assembly synthesis of Mn_3O_4/reduced graphene oxide hydrogel and its high electrochemical performance for supercapacitors. Chin J Chem 2013;31:1290–8.

[33] Wang D, Li Y, Wang Q, Wang T. Facile synthesis of porous Mn_3O_4 nano-crystal graphene nanocomposites for electrochemical supercapacitors. Eur J Inorg Chem 2012;4:628–35.

[34] Subramani K, Jeyakumar D, Sathish M. Manganese hexacyanoferrate derived Mn_3O_4 nanocubes–reduced graphene oxide nanocomposites and their charge storage characteristics in supercapacitors. Phys Chem Chem Phys 2014;16:4952–60.

[35] Frackowiak E, Beguin F. Carbon materials for the electrochemical storage of energy in capacitors. Carbon 2001;39:937–50.

[36] Liu HS, Song CJ, Zhang L, Zhang JJ, Wang HJ, Wilkinson DP. A review of anode catalysis in the direct methanol fuel cell. J Power Sources 2006;155:95–110.

[37] Park CY, Kefayat U, Vikram N, Ghosh T, OH WC, CHO KY. Preparation of novel CdS-graphene/TiO_2 composites with high photocatalytic activity for methylene blue dye under visible light. Bull Mater Sci 2013;36:869–76.

[38] Klug HP, Alexander LE. X-Ray diffraction procedures. New York: Wiley; 1970.

[39] (a). Liu TC, Pell WG, Conway BE. Self-discharge and potential recovery phenomena at thermally and electrochemically prepared RuO_2 supercapacitor electrodes. Electrochim Acta 1997;42:3541–52.

(b). Mohamed MM. Gold Loaded Titanium Dioxide Carbon Nanotube Composites as Active Photocatalysts for Cyclohexane Oxidation at Ambient Conditions. RSC Adv 2015;5:46405–14.

[40] Chu Y, Guo L, Xi B, Feng Z, Wu F, Lin Y, Liu J, Sun D, Feng J, Qian Y. Embedding MnO@Mn_3O_4 nanoparticles in an N-doped-carbon framework derived from Mn-organic clusters for efficient lithium storage. Adv Mater 2018;30:1704244.

[41] Peng BG, Cui JW, Wang Y, Liu JQ, Zheng HM, Jin L, Zhang XY, Zhang Y, Wu YC. CeO_{2-x}/C/rGO nanocomposites derived from Ce-MOF and graphene oxide as a robust platform for highly sensitive uric acid detection. Nanoscale 2018;10:1939–45.

[42] Fan Y, Zhou ZY, Feng Y, Zhou Y, Wen L, Shih KM. Degradation mechanisms of ofloxacin and cefazolin using peroxymonosulfate activated by reduced graphene oxide-$CoFe_2O_4$ composites. Chem Eng J 2020;383:123056.

[43] Qi XY, Pu KY, Li H, Zhou XZ, Wu SX, Fan QL, Liu B, Boey F, Huang W, Zhang H. Amphiphilic graphene composites. Angew Chem Int Ed 2010;49:9426–9.

[44] Wang HL, Robinson JT, Diankov G, Dai HJ. Nanocrystal growth on graphene with various degrees of oxidation. J Am Chem Soc 2010;132:3270–1.

[45] Cheng Q, Tang J, Ma J, Zhang H, Shinya N, Qin LC. Graphene and nanostructured MnO_2 composite electrodes for supercapacitors. Carbon 2011;49:2917–25.

[46] Nan CW, Shen Y, Ma J. Physical properties of composites near percolation. Annu Rev Mater Res 2010;40:131–51.

[47] Ibrahim I, Ali IO, Salama TM, Bahgat AA, Mohamed MM. Synthesis of magnetically recyclable spinel ferrite (MFe_2O_4, M = Zn, Co, Mn) nanocrystals engineered by sol gel-hydrothermal technology: high catalytic performances for nitroarenes reduction. Appl Catal B Environ 2016;181:389–402.

[48] Mohamed MM, Khairy M, Eid S. Activity and stability studies of titanates and titanate-carbon nanotubes supported Ag anode catalysts for direct methanol fuel cell. J Power Sources 2016;304:255–65.

[49] Portehault D, Cassaignon S, Baudrin E, Jolivet JP. Morphology control of cryptomelane type MnO_2 nanowires by soft chemistry. Growth mechanisms in aqueous medium. Chem Mater 2007;19:5410–7.

[50] Krishna MBM, Venkatramaiah N, Venkatesan R, Rao DN. Synthesis and structural, spectroscopic and nonlinear optical measurements of graphene oxide and its composites with metal and metal free porphyrins. J Mater Chem 2012;22:3059–68.

[51] Yang J, Wu M, Fei Z, Zhong M. Preparation, characterization, and supercritical carbon dioxide foaming of polystyrene/graphene oxide composites. J Supercrit Fluids 2011;56:201–7.

[52] Nethravathi C, Nisha T, Ravishankar N, Shivakumara C, Rajamathi M. Graphene nanocrystalline metal sulphide composites produced by A one-pot reaction starting from graphite oxide. Carbon 2009;47:2054–9.

[53] Bourlinos AB, Gournis D, Petridis D, Szabu T, Szeri A, Dekany I. Graphite oxide: chemical reduction to graphite and surface modification with primary aliphatic amines and amino acids. Langmuir 2003;19:6050–5.

[54] Jeong HK, Lee YP, Lahaye RJWE, Park MH, An KH, Kim IJ, Yang CW, Park CY, Ruoff RS, Lee YH. Evidence of graphitic AB stacking order of graphite oxides. J Am Chem Soc 2008;130:1362–6.

[55] Fu Y, Sun X, Wang X. $BiVO_4$–Graphene catalyst and its high photocatalytic performance under visible light irradiation. Mat Chem Phys 2011;131:325–30. Wang G, Huang B, Lou Z, Wang Z, Qin X, Zhang X, Dai Y. Valence State Heterojunction Mn3O4/MnCO3: Photo and Thermal Synergistic Catalyst. Appl Catal B: Environ. 2016; 180: 6–12.

[56] Kassaee MZ, Motamedi E, Majdi M. Magnetic Fe_3O_4-graphene oxide/polystyrene: fabrication and characterization of a promising nanocomposite. Chem Eng J 2011;172:540–9.

[57] Sayyed SG, Shaikh AV, Dubal DP, Pathan HM. Paving the way towards Mn_3O_4 based energy storage systems. ES Energy Environ 2021;14:3–21.

[58] Mousa MA, Khairy M, Shehab M. Nanostructured ferrite/graphene/polyaniline using for supercapacitor to enhance the capacitive behaviour. J Solid State Electrochem 2017;21:995–1005.

[59] Wu Y, Liu S, Wang H, Wang X, Zhang V, Jin G. A novel solvothermal synthesis of Mn_3O_4/graphene composites for supercapacitors. Electrochim Acta 2013;90:210–8.

[60] Mondal C, Ghosh D, Aditya T, Sasmal AK, Pal T. Mn_3O_4 nanoparticles anchored to multiwall carbon nanotubes: a distinctive synergism for high-performance supercapacitors. New J Chem 2015;39:8373–80.

[61] Dubal DP, Dhawale DS, Gujar TP, Lokhande CD. Effect of different modes of electrodeposition on supercapacitive properties of MnO_2 thin films. Appl Surf Sci 2011;257:3378–82.

[62] Zhang X, Sun X, Chen Y, Zhang DC, Ma YW. One-step solvothermal synthesis of graphene/Mn_3O_4 nanocomposites and their electrochemical properties for supercapacitors. Mater Lett 2012;68:336–9.

[63] Wang B, Park J, Wang CY, Ahn H, Wang GX. Mn_3O_4 nanoparticles embedded into graphene nanosheets: preparation, characterization, and electrochemical properties for supercapacitors. Electrochim Acta 2010;55:6812–7.

[64] Yang F, Zhao M, Suna Q, Qiao Y. A novel hydrothermal synthesis and characterisation of porous Mn_3O_4 for supercapacitors with high rate capability. RSC Adv 2015;5:9843–7.

[65] Gund GS, Dubal DP, Patil BH, Shinde SS, Lokhande CD. Enhanced activity of chemically synthesized hybrid

graphene oxide/Mn_3O_4 composite for high performance supercapacitors. Electrochim Acta 2013;92:205—15.

[66] Qian W, Chen Z, Cottingham S, Merrill WA, Swartz NA, Goforth AM, Clarec TL, Jiao J. Surfactant-free hybridization of transition metal oxide nanoparticles with conductive graphene for high-performance supercapacitor. Green Chem 2012;14:371—7.

[67] Liu C-L, Chang K-H, Hu C-C, Wen W-C. Microwave-assisted hydrothermal synthesis of Mn_3O_4/reduced graphene oxide composites for high power supercapacitors. J Power Sources 2012;217:184—92.

[68] Jin G, Xiao X, Li S, Zhao K, Wu Y, Sun D, Wang F. Strongly coupled graphene/Mn_3O_4 composite with enhanced electrochemical performance for supercapacitor electrode. Electrochim Acta 2015;178:689—98.

[69] Li L, Hu Z, Yang Y, Liang P, Lu A, Xu H, Hu Y, Wu H. Hydrothermal self-assembly synthesis of Mn_3O_4/reduced graphene oxide hydrogel and its high electrochemical performance for supercapacitors. Chin J Chem 2013;31:1290—8.

[70] Shuhua Y, Xuefeng S, Peng Z, Lian G. Crumpled nitrogen-doped graphene—ultrafine Mn_3O_4 nanohybrids and their application in supercapacitors. J Mater Chem 2013;1:14162.

[71] Subramani K, Jeyakumar D, Sathish M. Manganese hexacyanoferrate derived Mn_3O_4 nanocubes—reduced graphene oxide nanocomposites and their charge storage characteristics in supercapacitors. Phys Chem Chem Phys 2014;16:4952—61.

[74] Lee JW, Hall AS, Kim J-D, Mallouk TE. A facile and template-free hydrothermal synthesis of Mn_3O_4 nanorods on graphene sheets for supercapacitor electrodes with long cycle stability. Chem Mater 2012;24:1158—64.

[72] Du J, Gao Y, Chai L, Zou G, Li Y, Qian Y. Hausmannite Mn_3O_4 nanorods: synthesis, characterization and magnetic properties. Nanotechnol 2006;17:4923—30.

[73] Nam KW, Kim KB. Manganese oxide film electrodes prepared by electrostatic spray deposition for electrochemical capacitors. J Electrochem Soc 2006;153:A81—8.

[75] Cheng H, Duong HM, Jewell D. Three dimensional manganese oxide on carbon nanotube hydrogels for asymmetric supercapacitors. RSC Adv 2016;6:36954—60.

[76] Khairy M, Faisal K, Mousa MA. High-performance hybrid supercapacitor based on pure and doped $Li_4Ti_5O_{12}$ and graphene. J Solid State Electrochem 2017;21:873—82.

[77] Balasubramaniam M, Balakumar S. Exploration of electrochemical properties of zinc antimonate nanoparticles as supercapacitor electrode material. Mater Sci Semicond Process 2016;56:287—94.

[78] Daniel V. Dielectric relaxation. London and New York: Academic Press; 1967.

[79] Boukamp BA. A Nonlinear Least Squares Fit procedure for analysis of immittance data of electrochemical systems. Solid State Ionics 1986;20:31—44.

[80] Macdonald JR, editor. "Impedance spectroscopy". New York, USA: John Wiley & Sons; 1987.